Control of an Inflatable Robotic Manipulator

João Pedro Ribeiro de Oliveira
joao.pedro.oliveira@tecnico.ulisboa.pt

Instituto Superior Técnico, Universidade de Lisboa
Lisboa, Portugal

June 2017

Abstract

This thesis involves the feasibility of using an optical flow sensor in order to detect the vibrations of an inflatable link robot end effector. A survey of the current state of the art in soft robotics, optical flow and the motivation and scope of this thesis is introduced. Also a communication pathway was designed, to build a bridge between the ADNS-3080 optical flow sensor and the Simulink Real-Time target computer. This was achieved by implementing an Arduino Uno microcontroller board with an Ethernet Shield to complete the path. As a main advantage, this noninvasive sensor does not change the mechanical properties of the inflatable link. A model was developed using a lumped parameter model to explain the dynamics of the inflatable link robot, to predict its behavior under position and vibration control. Finally, the vibration control performance in the two cartesian directions of the spherical workspace of the inflatable link robot is shown in the results chapter. This results show that it is possible to implement a vibration control solution with feedback information from the ADNS-3080.
Keywords: Soft Robotics, Inflatable Link Robot, Optical Flow, ADNS-3080, Vibration Control.

1. Introduction

The motivation for this thesis stems from the work previously developed by Ferreira [1], where the goal was to design, build and control a prototype of an inflatable robotic manipulator. In this previous prototype, a webcam was connected via USB was used to obtain information about the non-invasive inflatable link oscillations. This webcam presented limitations with respect to a delay of 100 milliseconds and a number of frames per second (FPS) of 30.

Flexible robotics aims to make robots intrinsically more secure. These present less weight, as in [6], so potential damages will be much reduced. Since these robots are complacent with the medium where they operate given their structure being flexible.

In several previous works, such as [10, 20], this type of multi-load structure has been tested to study the applicability limits of the Euler-Bernoulli model.

In the study [22] where a non-linear model was developed, which allows to explain the wrinkling of the structure in non-linear deformation. In more recent studies [24, 23], these nonlinearities were studied in the perspective of taking advantage of them. Thus, being able to develop a kinematic model of the robot using the link wrinkle as a joint to change its configuration in space.

Based on all this research work it has been possible to develop a series of robotic arms over the years that find their applications in interaction with humans, among them presented in [18, 23, 17, 15, 14, 9] , As well as a fully inflatable pneumatic actuated humanoid shown in [5].

In recent years, optical flow has had applications within mobile robotics by estimating the position of the robot for locating and navigating within unstructured spaces as exemplified in [19]. With commercial optical flow sensors it is also possible to control and map robots in space, as in [4, 7]. One of the most interesting applications in this field is the prevention and detection of obstacles [25]. It is possible to verify an application of ADNS-3080, optical flow sensor in simultaneous localization and mapping (SLAM) [13].

The application under this thesis is innovative, since in this case it refers to the detection of vibrations of an inflatable robot link actuated by servo motors.

However, in this work we will explore these limitations in order to guarantee the maximum performance of the inflatable robotic manipulator. Since the characteristics presented by the USB webcam have proved to be insufficient, in this thesis will be explored the application of a commercial optical flow sensor, the ADNS-3080.

2. Experimental Setup

In this section, the structure which composes the robotic inflatable arm and its mechanical and electromechanical upgrades are shown. Later in this section is also presented the instrumentation used and the communication pathway implemented. With this in mind, the prototype was redesigned to: Support both cameras the ADNS-3080 and a new web cam over the printed circuit board (PCB) that allows an interface between the sensors and the control system; Allow a better seal of the air, avoiding leaks; Improving the mechanical coupling resistance.

2.1. Prototype

In this figure 1, it is possible to compare the real prototype with its computer assisted design (CAD) rendering.

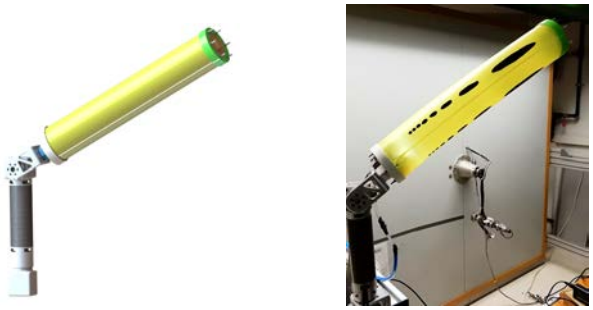

(a) CAD Render (b) Real Prototype

Figure 1: Prototype structure.

In order to schematize the experimental system as a whole we have the figure 2, where the main components of this prototype are represented.

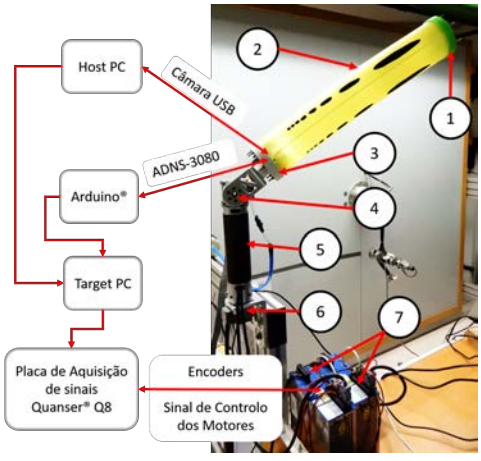

Figure 2: Prototype Scheme.

According with the figure enumeration, it is possible o present a bill of materials of this prototype: Top support; Polyurethane inflatable link; Base support that holds the web cam and the ADNS-3080; Servo Motor, joint 2; Carbon fiber link; Servo Motor, joint 1 and Harmonic Drive® Amplifiers.

2.1.1 Air seal

Based on the prototype design an o-ring rubber gasket was applied to reduce the possibility of air leaks from inside the inflatable, figure 3.

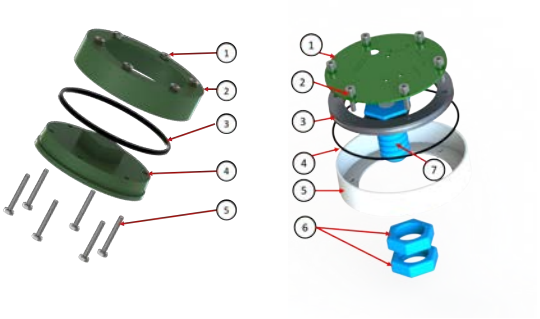

(a) Top (b) Base

Figure 3: O-ring application.

Here is the list of parts of the top set in the figure 3 a): six nuts M4, top part that closes the inflatable, *O-ring*, terminal element of robotic arm, six M4 screws.

Here is the list of parts of the base assembly in figure 3 b): printed circuit board, six M4 screws, mechanical coupling bracket to servo motor arm, *O-ring*, part that closes the base of the inflatable arm, two M22 nuts for the mechanical connection to the servo motor arm, a M22 bolt for the mechanical connection to the arm of the servo motor reinforced with steel rod inside.

2.1.2 Mechanical coupling

In order to attach the inflatable base to the servo motor arm, a M22 nut and an M22 bolt were printed on a 3D printer in PLA. After that was applied a reinforcement with an insert in solid steel, on the inner part of the bolt. In this way guaranteeing the mechanical resistance of this connection, figure 4.

Figure 4: 3D Printed bolt reinforced with a steel insert.

2.1.3 Electric circuit

For manufacturing a printed circuit board that would make the necessary connections and isolate the air inside the inflatable link. A circular printed circuit board was designed to connect the sensors to the control system outside of the link, figure 5.

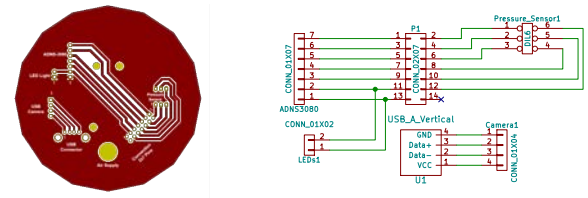

(a) Design (b) Schematic

Figure 5: PCB Schematic and design.

2.2. Instrumentation

The group of sensors choose for the inflatable robotic manipulator are described in this section.

2.2.1 Pressure System

The pressure control system is composed of a mini-pump WP36C-12N and a pressure sensor series MPS-3100. Which uses a power source up to 12 V with a 0.9 A current and to maximum pressure of 80 kPa.

The MPS-3117-006GC [11] was the pressure sensor implemented on this new version of the prototype. Which has linear pressure range between 0 kPa and 44 kPa. It is a highly sensitive resistive sensor of 5 $k\Omega$.

This sensor has an analog output of 400 mV to 550 mV, this signal will be read in an analog input from 0 V to 8 V. The analog input of the Quanser® allows a upper limit of 10 V but in order to avoid problems of saturation of it, we chose the above mentioned interval.

With this goal in mind a signal conditioning circuit with LM741 operational amplifiers had been developed. This consists of two non-inverting amplifier circuits and a subtractor circuit with a gain of 55.6 with the resistors presented in the figure 6, $R_2 = 5.56\,k\Omega$, $R_1 = 100\,\Omega$.

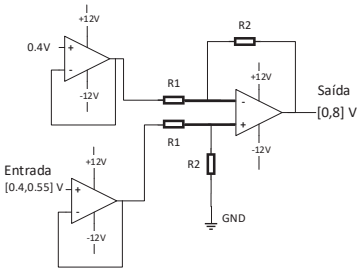

Figure 6: Signal conditioning circuit.

2.2.2 Webcam

At the base of the robotic arm was installed a camera, the Trust Spotlight Webcam aligned with its axis of revolution, figure 7.

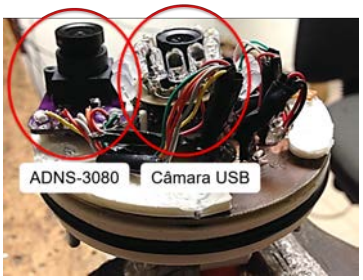

Figure 7: Webcam mounted at the center and the ADNS-3080 mounted on the left side.

To guarantee a minimum number of frames at 30 FPS, a resolution of 320 by 240 pixels was used.

This camera was installed with two purposes, the first one to perform on a collision detection algorithm as in [1] and the second to obtain a calibration for the ADNS-3080, optical flow sensor, shown in section 2.2.3.

2.2.3 Optical flow sensor ADNS-3080

The ADNS-3080 is an optical flow sensor of an optical computer mouse consisting of a low resolution camera and a signal processing system that estimates relative displacement by applying a comparative analysis to a sequence of acquired images.

According to the manufacturer, Avago Technologies [3], the ADNS-3080 can process from 2000 to 6469 FPS, with a resolution of 30 by 30 pixels, figure 8.

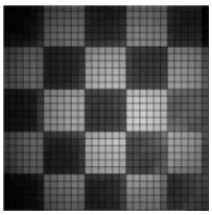

Figure 8: ADNS-3080 Image size.

The ADNS-3080 provides three values: δ_x, δ_y and surface quality. The latter corresponds to a quarter of the number of features detected in the reading, which has a maximum value of 169. So that reaching the actual displacement velocity value we have the following equation (1), which has the field of view, fov, in radians, height, h, in millimeters and the resolution of the sensor, r, in pixels.

$$V_{x/y} = \frac{\delta_{x/y}}{r} \cdot h \cdot 2 \cdot \tan\left(\frac{fov}{2}\right) \qquad (1)$$

The above equation can be simplified by replacing the constants of the equation by a calibrated gain with the webcam referred in the section 2.2.2.

2.2.4 Targets

In the figure 9, the circular target that has a surface quality value of 85 is shown for a maximum of 169 as presented in the previous section 2.2.3.

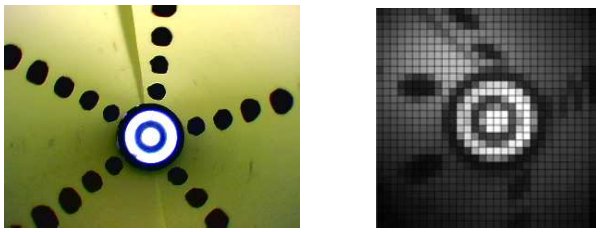

(a) Webcam Image (b) ADNS-3080 Image

Figure 9: Concentric rings target.

For the second target was chosen a matrix of squares that should be more interesting features to focus the sensor at the desired distance. In the figure 10, the target that has a value of 80 for the surface quality, this is due to the less detail seen in the ADNS-3080 image.

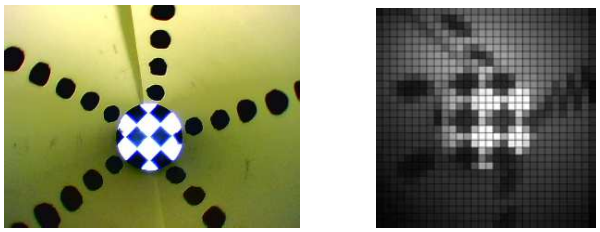

(a) Webcam Image (b) ADNS-3080 Image

Figure 10: Matrix of squares target.

One of the most critical issues on the installation of the ADNS-3080 was the illumination needed inside of the prototype so that it detects the target of the link, which is enough to saturate the sensor of the webcam, as it can be seen in the figures 9 and 10.

In both images of the ADNS-3080, the target occupies a small portion of the image, this is detrimental to achieve a satisfactory resolution, so that it would be necessary to explore other lenses in order to decrease the field of view of the sensor.

However, despite these limitations, the circular target was used to obtain the results of this thesis. In favor of the computational vision algorithm implemented in the 2.2.6 section.

2.2.5 Delay characterization

As a means of achieving a complete characterization of the sensors installed in the prototype, it is necessary to collect information about the delays of the system in the capture of oscillations of the inflatable link. In order to determine the delay of the image capture by the two cameras installed in the prototype, an accelerometer was provisionally installed that provided an analog signal to the signal acquisition plate, enabling the measurement of camera delay in response to an impulse in the horizontal direction corresponding to the direction y. As a result of this experience, we can say that there has been a significant improvement with the update of the webcam by a modern model with a delay of 35 ms, and the ADNS-3080 has a delay of 27 ms, which is small enough for the application under study in this thesis, Comparing this result with that of the previous thesis [5], in which the chamber had a delay of 100 ms.

2.2.6 Calibration

In order to compare the real position obtained through the webcam and the position integrating the speed obtained at each instant by the ADNS-3080, it is necessary to previously obtain the calibration of the camera [16].

Based on what was done in [1], it is possible to obtain the prototype end effector detection algorithm, figure 11.

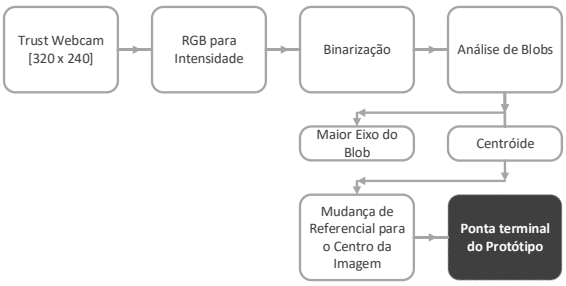

Figure 11: End effector detection algorithm.

In this algorithm we can through the largest axis of the Blob (corresponding to the diameter of the largest circular ring, figure 9) detected compare with the actual size of the target. By this obtaining an experimental gain, $k_{cam} = 1,021$ that we can apply to the webcam values.

As a result of the experiments described in this section we obtained a gain for each of the directions, $k_x = 0.25524$ and $k_y = 0.22452$ through a linear regression between the displacements detected with the ADNS-3080 (sensor values were integrated according to their sample time) and those detected

with the webcam.

So that we should update the equation (1) to:

$$V_{x/y} = k_{x/y} \cdot \delta_{x/y} \tag{2}$$

2.2.7 Communication

The solution proposed in this thesis to ensure communication between sensors and actuators is the Simulink with a real-time simulation tool. This software is used to ensure that the control is done in real-time with a sampling time of 1 ms. To ensure that the simulation is done with a minimum error in relation to the real-time, two computers are required:

- The Target where the simulation is run, the sensors are read and the motors are actuated.
- The Host where the Simulink file that will run in the Target is compiled and where the final simulation results are acquired.

In the case of this thesis, the Target does not have a Universal Serial Bus (USB) interface, it is necessary to run the vision algorithm inside the Host, by making a parallel UDP communication to the existing TCP between the Target and the Host.

The main electronic components that compose the communication pathway are:

- Quanser® Q8 .
- Arduino® Uno.
- Arduino® Ethernet Shield.

The *Quanser® Q8* is a control and signal acquisition board which is compatible with Simulink. This allows simultaneous operation of the servo motors and the air compressor, as well as reading the encoders of the servo motors and the pressure sensor MPS-3117.

The Arduino® Uno is a prototyping board that allows you to expand the features of its reprogrammable microprocessor, the ATmega328/P. In the context of this thesis, Arduino® bridges the ADNS-3080 and Arduino® Ethernet Shield. To do this, it is necessary to use a protocol compatible with ADNS-3080, the Serial Peripheral Interface (SPI), that works in a master-slave perspective and is a synchronous serial interface with a single master and multiple slaves as long as the peripherals, slaves, use the same communication configurations between them.

The ADNS-3080 uses the SPI protocol in mode 3 and the Arduino® Ethernet Shield in mode 0. Therefore, it is necessary to use two masters, in order to achieve this objective. It is necessary to emulate a second SPI protocol within the Arduino® Uno, using a Universal Synchronous Asynchronous Receiver Transceiver (USART) protocol in SPI mode. This mode is described in detail in the processor manufacturer's manual, ATmel® [2].

With the aid of an analyzer and a logical decoder from the manufacturer Saleae®, we can see in detail the two protocols in operation, by decoding hexadecimal messages, figure 12.

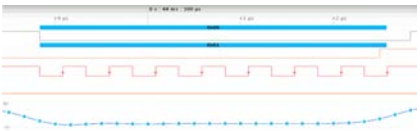

(a) Arduino® and ADNS-3080

(b) Arduino® e Arduino® Ethernet Shield

Figure 12: Saleae® analyzer and a logical decoder.

After sending the packet to Arduino® Ethernet Shield successfully completed it must be sent to Target. In order to complete this task, the user datagram protocol (UDP) was chosen instead of the Transmission Control Protocol (TCP), since the objective is stream, sending Continuously regardless of whether there is a receipt from the Target part, as mentioned in the previous work [8].

The critical feature of any communication system is its bottleneck transmission speed, which is the path that connects the optical flow sensor to the Target, which in this case is found in Arduino® Ethernet Shield that limits the velocity to 90 Hz, figure 13. This is due to the low frequency with which the driver of the ethernet port can activate or deactivate the shield each time it is necessary to send a packet via UDP.

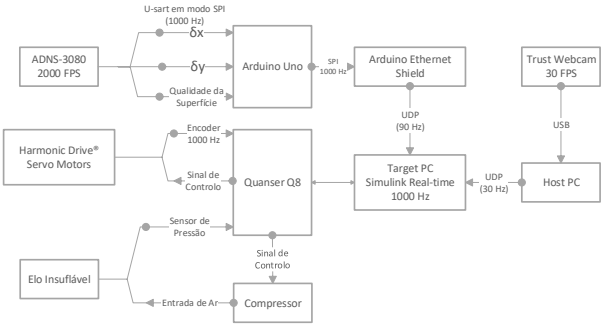

Figure 13: Communication Overview.

3. Modeling and Control

In this section will be approached the modeling of the dynamic system of the inflatable arm as well

as the control systems necessary for the operation of the prototype.

3.1. Dynamic Model

The inflatable arm is modeled based on a lumped parameter model. The dynamic model of the system was performed with mass, spring and damper components, as in[12, 21].

This model is presented in the figure 14 by the linear equivalent, for ease of representation in relation to the angular sytem. This consists of the inertia of the actuator I_m, the inertia of the link I (modeled the mass of a pendulum), joint angle θ_1, inflatable arm end effector angle θ_2, motor damper c (representing joint friction), the spring and damper assembly, respectively k and b, representing the link dynamics.

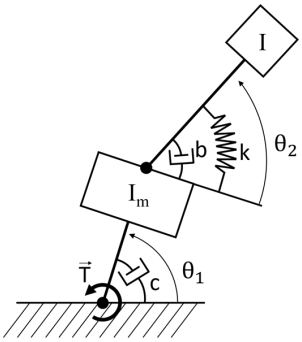

Figure 14: System Model Representation.

This system is modeled with two balance of forces, equation (3), around each of the inertias present in the figure 14.

$$\begin{cases} I_m\,\ddot{\theta_1} + c\,\dot{\theta_1} = T + b\,(\dot{\theta_2} - \dot{\theta_1}) + k\,(\theta_2 - \theta_1) \\ I\,\ddot{\theta_2} = b\,(\dot{\theta_1} - \dot{\theta_2}) + k\,(\theta_1 - \theta_2) \end{cases} \tag{3}$$

Considering $\delta\theta = \theta_2 - \theta_1$ comes the equation (4).

$$\begin{cases} I_m\,\ddot{\theta_1} + c\,\dot{\theta_1} = T + b\,\dot{\delta\theta} + k\,\delta\theta \\ -I\,\ddot{\theta_1} = I\,\ddot{\delta\theta} + b\,\dot{\delta\theta} + k\,\delta\theta \end{cases} \tag{4}$$

By applying the Laplace transform to the equation (4), we can make the equation (5).

$$\begin{cases} \theta_1(s)\,(I_m\,s^2 + c\,s) = T(s) + \delta\theta(s)\,(b\,s + k) \\ \theta_1(s)\,(-I\,s^2) = \delta\theta(s)\,(I\,s^2 + b\,s + k) \end{cases} \tag{5}$$

Substituting the second line of the equation (5) in the first one, eliminating the variable θ_1 and solving in order to obtain the transfer function of $T(s)$ to $\delta\theta(s)$ in the equation (6).

$$\frac{\delta\theta(s)}{T(s)} = \frac{-I\,s}{I \cdot I_m\,s^3 + (b\,(I + I_m) + I\,c)\,s^2 + (k\,(I + I_m) + b\,c)\,s + k\,c} \tag{6}$$

Substituting the second line of the equation (5) in the first, eliminating the variable $\delta\theta$ and solving in order to obtain the transfer function from $T(s)$ to $\theta_1(s)$ In the equation (7).

$$\frac{\theta_1(s)}{T(s)} = \frac{I\,s^2 + b\,s + k}{I \cdot I_m\,s^4 + (b\,(I + I_m) + I\,c)\,s^3 + (k\,(I + I_m) + b\,c)\,s^2 + k\,c\,s} \tag{7}$$

The model parameters are resumed in the table 1.

Table 1: Model parameters at the pressure of 18 kPa.

I_m	$2.9 \times 10^{-6}\ kg \cdot m^2$
c	$5.3 \times 10^{-3}\ N \cdot m \cdot rad/s$
I	$0.0238\ kg \cdot m^2$
k	$9.422\ N/rad$
b	$0.061\ N \cdot s/rad$

In this section we obtain the two transfer functions that govern the two variables we want to control, $\delta\theta(s)$ and $\theta_1(s)$ with the input of the motors the torque $T(s)$:

- The first represents the vibration of the system, presenting a non-minimal phase behavior of the link in response to a torque input value.
- The second represents the influence of joint dynamics, including the influence of vibration in response to an inlet torque to the joint.

3.2. Pressure Control

This controller is composed by a $P = 35$ and $D = 2$.

In order to validate the operation of this controller it is possible to observe the response to the step, in the figure 15. This controller is validated with a settling time of 5% of 4.48 seconds and a steady position error of 460 Pa.

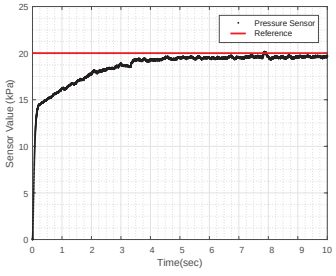

Figure 15: Step response of the pressure controller.

3.3. Position Control

To achieve the desired control solution, it is necessary to add, by means of the superposition principle, the actuation corresponding to the joint po-

sition control to the operation of the vibration control. The joint position control is done based on the transfer function (7), presented in section 3.1 referring to the modeling of the system, which describes the influence of the inflatable on the joint.

The solution for joint position control, presented in [1], with a proportional component of 82.1 and a derivative component of 3.6, was validated in the prototype by means of the response to a step.

The response to a step with this controller is represented in figure 16, with a maximum overshoot of 0.13%, establishment time of 2% of 0.37 seconds and a steady position error of 0.005 radians.

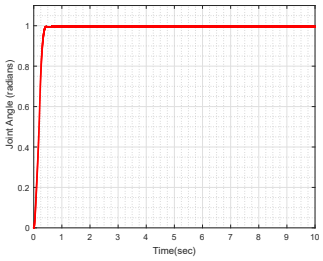

Figure 16: Step response of the position control.

3.4. Vibration Control

In order to guarantee the accuracy of the robotic arm, it is necessary to deal with the problem of inflatable link vibrations. Due to oscillatory behavior it is necessary to operate the joint in order to reduce vibrations, as shown in figure 17.

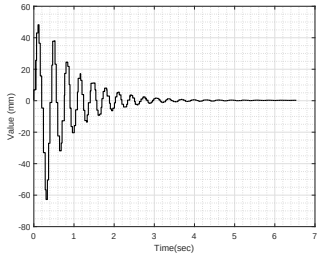

Figure 17: Oscillatory behavior of the inflatable link.

With ADNS-3080 we obtain velocity information, $\dot{\delta\theta}$, since the prototype is actuated with the derivative information of $\delta\theta$ it is necessary to use the transfer function (6), here identified as $G_1(s)$ in the equation (8).

$$G_1(s) = \frac{\delta\theta(s)}{T(s)} \tag{8}$$

The final vibration control transfer function, $G(s)$, after the negative feedback, equation (9):

$$G(s) = \frac{P \cdot G_1(s)}{1 + P \cdot s\, G_1(s)} \tag{9}$$

The gain, P, referred above for the direction X it is 70 and for the direction Y it is 90.

4. Results

In this thesis, we are able to test the feasibility of implementing a commercial optical flow sensor for the task of vibration damping associated with the oscillatory movement of the inflatable robot arm end effector, in both directions (X and Y) of a spherical workspace. It is possible to overcome the limitations presented in previous work [1], specifically the ones related to the webcam.

In order to achieve this results the prototype was actuated with a cubic trajectory to guarantee operation within the saturation levels, figure 18

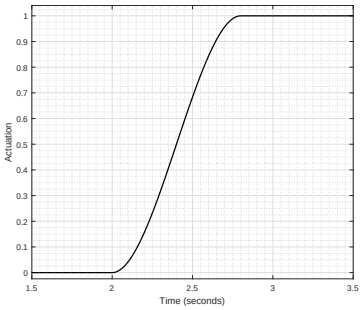

Figure 18: Cubic trajectory

4.1. Vibration

For the study of vibration control performance, the time response of an one radian step is presented, in three different cases of actuation: on the vertical direction, on the way of gravity (Case 1); on the vertical direction, in the opposite way to gravity (Case 2); on a horizontal direction (Case 3); simultaneous actuation of both joints (Case 4).

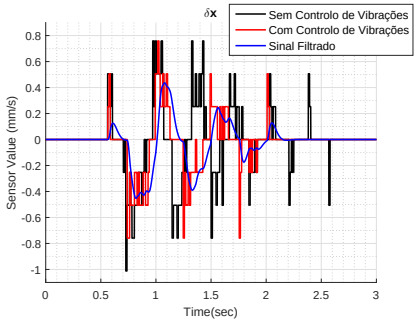

Figure 19: δ_x obtained with ADNS-3080. Case 1

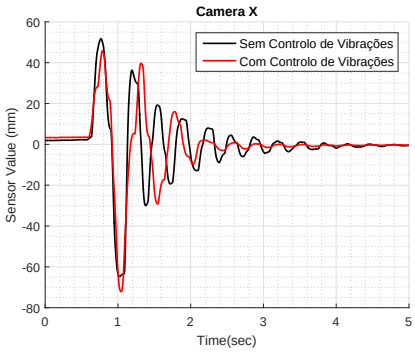

Figure 20: X obtained with the webcam. Case 1

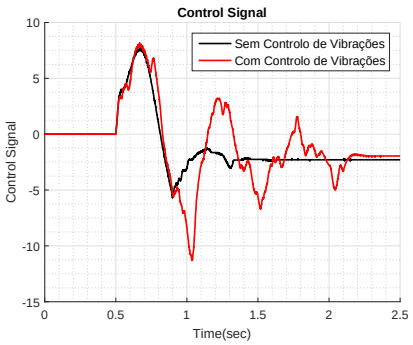

Figure 21: Control signal. Case 1

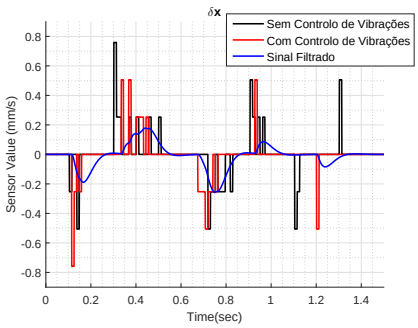

Figure 22: δ_x obtained with ADNS-3080. Case 2

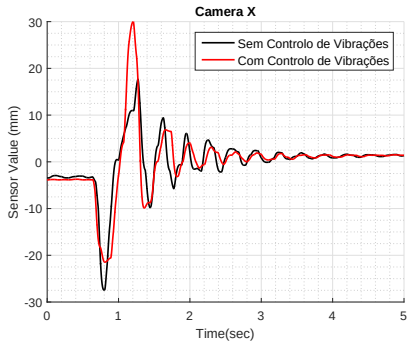

Figure 23: X obtained with the webcam. Case 2

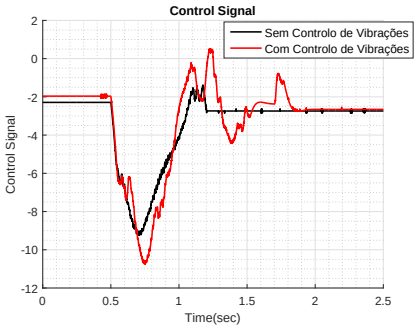

Figure 24: Control signal. Case 2

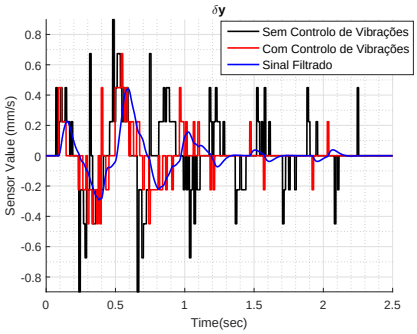

Figure 25: δ_y obtained with ADNS-3080. Case 3

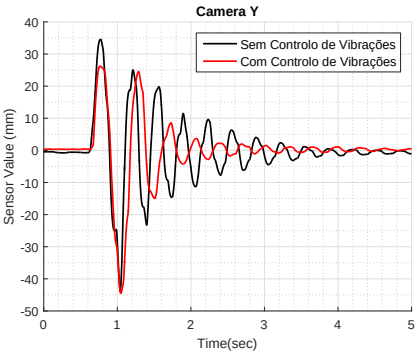

Figure 26: Y obtained with the webcam. Case 3

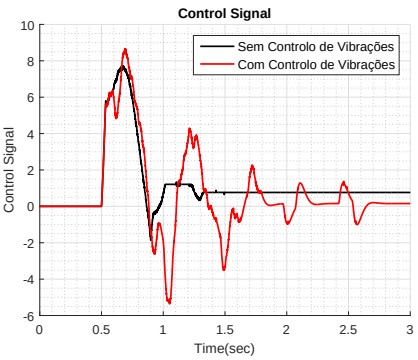

Figure 27: Control signal. Case 3

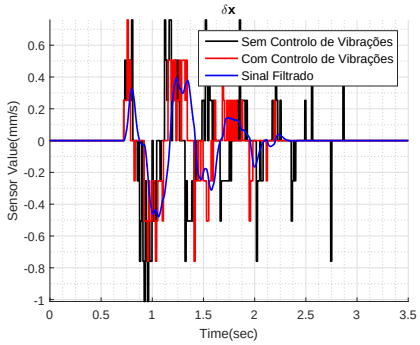

Figure 28: δ_x obtained with ADNS-3080. Case 4

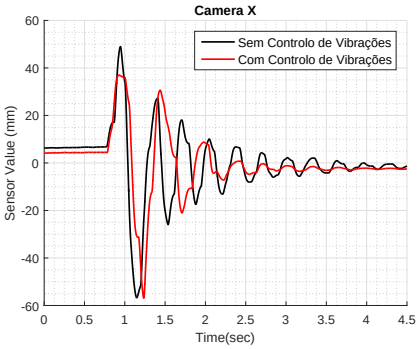

Figure 29: X obtained with the webcam. Case 4

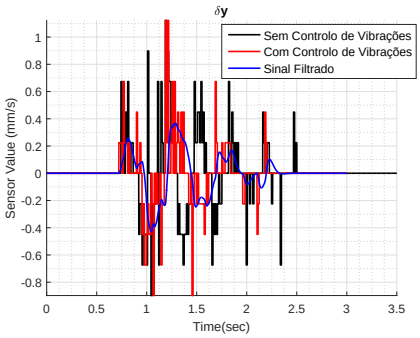

Figure 30: δ_y obtained with ADNS-3080. Case 4

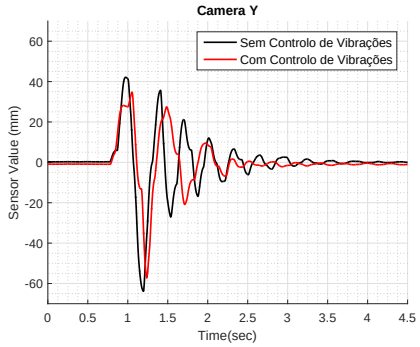

Figure 31: Y obtained with the webcam6. Case 4

It is to be noticed that on the case 1, we have good attenuation of the arm tip oscillations. However, on the case 2 we have a really low resolution from the filtered signal of the ADNS-3080, which leads to worse result in terms of damping. On the third case, the controller actuation increases the settling time of the oscillatory behavior. On the forth case, we have the most similar result to operation in real world tasks, where we can achieve some damping reflected of attenuation of frequency of oscillation.

5. Conclusions

Communication was established between ADNS-3080 and the Target computer, through an Arduino® Uno and an Arduino® Ethernet Shield.

Improvements were applied to the mechanical structure, in order to have a proper coupling to the servo motor arm.

To reduce leaks in the inflatable robot arm and to improve the electrical connection capabilities between the interior of the prototype and its exterior.

The vibration control can dampen the oscillations even though in some cases only a satisfactory attenuation is achieved in a timely manner. This damping is reflected both in the reduction of wave amplitude and in the reduction of vibration frequency.

Within the tests performed with the ADNS-3080 is the characterization of the behavior of the optical flow sensor to circular targets and to square matrix targets. These showed a better focus of the resulting image for the circular target, verifying a number of higher detected characteristics.

However, the sensor readings are somewhat scattered and of low resolution, that is, the displacement of a 1-radian step from the prototype represents only 10 speed levels which proved to not be a satisfactory resolution. If a lens is applied that allows a smaller field of view that can substantially improve the performance of the sensor for this type of application.

Acknowledgements

I wish to thank all my colleagues, my dearest family and my girlfriend, for their constant support.

I wish also to thank to the professors and laboratory staff who helped me throughout this thesis.

Last but not least to my supervisor Prof. João Carlos Prata dos Reis, that without his full support, orientation, dedication and availabity this thesis would not be possible.

References

[1] Afonso Clara Pinto Ferreira. Inflatable structures for Robotic Applications. Master's thesis, Instituto Superior Técnico, Lisboa, 2016.

[2] Atmel. Datasheet, ATmega328/P, 8-bit AVR Microcontrollers.

[3] Avago. Datasheet, ADNS-3080 High-Performance Optical Mouse Sensor. 2008.

[4] R. L. Barbosa, R. Bezerra, D. A. Gallis, and J. Fernando. A computação do fluxo óptico em imagens obtidas por um sistema móvel de mapeamento terrestre. *Revista Brasileira de Cartografia*, 57(02):72–78, 2005.

[5] C. M. Best, J. P. Wilson, and M. D. Killpack. Control of a pneumatically actuated, fully inflatable, fabric-based, humanoid robot. *IEEE-RAS International Conference on Humanoid Robots*, 2015-Decem:1133–1140, 2015.

[6] J. M. G. dos Santos Mendes. Integrated Design of Lightweight Robot Manipulators. Master's thesis, Instituto Superior Técnico, Lisboa, 2009.

[7] M. Filho, H. Schneebeli, and E. Caldeira. Cálculo do fluxo ótico em tempo real e sua utilização na navegação de robôs móveis. Universidade Federal do Espírito Santo. 2001.

[8] D. F. d. C. Gonçalves. Implementação e Validação de Interfaces de Reconhecimento Gestual para Utilização em Cirurgias de Invasão Mínima Engenharia Mecânica. Master's thesis, Instituto Superior Técnico, Lisboa, 2016.

[9] H. J. Kim, Y. Tanaka, A. Kawamura, S. Kawamura, and Y. Nishioka. Development of an inflatable robotic arm system controlled by a joystick. *Proceedings - IEEE International Workshop on Robot and Human Interactive Communication*, 2015-Novem:664–669, 2015.

[10] J. A. Main, S. W. Peterson, and A. M. Strauss. LoadDeflection Behavior of SpaceBased Inflatable Fabric Beams. *Journal of Aerospace Engineering*, 7(2):225–238, apr 1994.

[11] Metrodyne Microsystem Corp. Datasheet, MPS-3110 series Pressure Sensor.

[12] M. Östring. Identification, Diagnosis, and Control of a Flexible Robot Arm. Master's thesis, Link oping Studies in Science and Technology, Sweden, 2002.

[13] R. Paper, N. Gageik, M. Strohmeier, and S. Montenegro. An Autonomous UAV with an Optical Flow Sensor for Positioning and Navigation. *International Journal of Advanced Robotic Systems*, pages 1–9, 2013.

[14] R. Qi, T. L. Lam, and Y. Xu. Kinematic modeling and control of a multi-joint soft inflatable robot arm with cable-driven mechanism. *Proceedings - IEEE International Conference on Robotics and Automation*, pages 4819–4824, 2014.

[15] R. Qi, T. L. Lam, and Y. Xu. Mechanical design and implementation of a soft inflatable robot arm for safe human-robot interaction. *Proceedings - IEEE International Conference on Robotics and Automation*, pages 3490–3495, 2014.

[16] J. C. Reis. Estudo da dinâmica de um corpo em movimento por visão computacional. Master's thesis, Instituto Superior Técnico, Lisboa, 2001.

[17] N. Salomonski, M. Shoham, and G. Grossman. Light Robot Arm Based on Inflatable Structure. *CIRP Annals - Manufacturing Technology*, 44(1):87–90, 1995.

[18] S. Sanan. *Soft Inflatable Robots for Safe Physical Human Interaction*. PhD thesis, The Robotics Institute Carnegie Mellon University, Pittsburgh, 2013.

[19] D. K. Sorensen, M. Ovinis, and S. Lee. On-Line Optical Flow Feedback. (October), 2003.

[20] J. D. Suhey, N. H. Kim, and C. Niezrecki. Numerical modeling and design of inflatable structuresapplication to open-ocean-aquaculture cages. *Aquacultural Engineering*, 33(4):285–303, 2005.

[21] D. Tsetserukou, N. Kawakami, and S. Tachi. Vibration damping control of robot arm intended for service application in human environment. *IEEE-RAS International Conference on Humanoid Robots*, 1:441–446, 2008.

[22] S. L. Veldman. *Design and analysis methodologies for inflated beams*. 2005.

[23] S. Voisembert. *Design and modeling of an ultra lightweight robotic inspection arm*. PhD thesis, ParisTech, 2012.

[24] S. Voisembert, A. Riwan, N. Mechbal, and A. Barraco. A novel inflatable robot with constant and continuous volume. *Proceedings - IEEE International Conference on Robotics and Automation*, pages 5843–5848, 2011.

[25] Z. Wei. *Real-Time Optical Flow Sensor Design and its Application on Obstacle Detection*. PhD thesis, Brigham Young University, 2009.